The size and lifetime of organised eddies in a non-solid-body rotating turbulence experiment

L. Gan, Andrea Maffioli

The size and lifetime of organised eddies in a non-solid-body rotating turbulence experiment

Gan L.[a,*], Maffioli A.[b]

[a] *Department of Engineering, Durham University, DH1 3LE, UK*
[b] *Laboratoire de Mécanique des Fluides et d'Acoustique, Ecole Centrale de Lyon, 69134 Ecully, France*

Abstract

This paper follows our previous study of forced non-solid-body rotating turbulence and summarises results on the eddy size and lifetime in the same flow. The experiment is conducted in a dodecagonal tank ($R_t \approx 1$m in radius and 2m in height) and the bulk rotation is onset by the co-rotation of two circular impellers installed on the top and the bottom of the tank. Turbulence is continuously injected to the central region mainly from the vertical baffles installed on the tank wall. As the impellers rotate in a steady manner, the global Reynolds number (Re_G) and Rossby number (Ro_G) sustain in the range of $350 \sim 5900$ and $1.44 \sim 3.35$ respectively. Two-dimensional particle image velocimetry (2DPIV) measurements are carried out in a plane normal to the axis of the rotation and in the central region of the tank, where the flow is found Rayleigh stable. By developing an eddy detection and a lifetime estimation algorithm, we show that there seems to be a characteristic eddy size d^*, which is about $0.08 \sim 0.1R_t$ and is weakly dependent on Re_G. Among eddies which are smaller than d^*, anti-cyclonic ones are dominant, but only marginally, while for eddies larger than d^*, prevalence of cyclonic eddies is evident in both number density and lifetime. The demarcation eddy size d^* corresponds to approximately constant values of macro Rossby number $Ro^* \approx 2$ and micro Rossby number $Ro^*_\omega \approx 8$ at high Re. This is consistent with the case of solid-body rotating turbulence and indicates that the cyclonic prevalence is here also due to the centrifugal instability, which preferentially depletes anti-cyclones at $Ro \sim 1$. On average, the longest lived eddies are found to be of $d \approx 1 \sim 1.5d^*$ and have life spans which are an order of magnitude larger than the turbulence eddy turn over time. The local Ro, defined based on the local flow rotation rate and local averaged size of organised cyclonic eddies, is found to be self-adjusted to $2.75 \sim 3.75$, inside which the maximum extent of cyclonic eddy predominance, measured by the vorticity skewness, is observed. This brings about that the average size of the cyclonic eddies at a given radius is $\langle d \rangle \sim u_r/\Omega_r$ (where u_r and Ω_r are the local fluctuating velocity and local rotation rate), which is found to be an important scale in this problem.

Keywords: non-solid-body rotating turbulence, forced steady, experiments

1. Introduction

Turbulence in a rapidly rotating environment is often characterised by Reynolds number $Re = ul/\nu$ and Rossby number $Ro = u/\Omega l$, where u is the characteristic fluctuating velocity scale and l is a suitably defined length scale. In applications where the viscous effect can be neglected, e.g. medium to high Re, Ro becomes the governing parameter. Ro is a measure of the ratio of inertial to rotational effects. In such flows, coherent flow structures spontaneously emerge in a form of organised long columnar eddies aligned with the axis of bulk rotation, with the cyclones (spin in the same direction of the bulk rotation) predominant over the anti-cyclones (spin in the opposite direction) [8]. The feature becomes overwhelming as Ro drops from high to $O(1)$, reflected by the strong skewness of vorticity towards cyclonic side [10, 13]. These columnar eddies are also found to be responsible for suppressing the turbulence decay rate, compared to non-rotating homogeneous turbulence [13]. In an unbounded environment (or a large bounded one), the

*Email: lian.gan@durham.ac.uk

(cyclonic) eddy characteristic diameter becomes a suitable length scale available in the flow, which is conventionally chosen to be the length scale l for Re and Ro.

There have been two mechanisms proposed to explain the emergence of columnar eddies in rotating turbulence. In flows where $Ro \sim 1$ and Re is not too low, it was attributed to either inertial wave propagation [3, 2, 9] which is supported by experiments [13] and numerical studies [12] or non-linear wave interaction theory [14], which is also consistent with findings in [11]. The real formation process is thus probably the complex combination of the two mechanisms; see Davidson et al. [4] Chapter 8 for more discussions.

The prevalence of cyclonic eddies over anti-cyclonic eddies in rotating turbulence has been reported in experiments [8, 10, 13] and numerical simulations [1, 5] of the problem. This cyclone/anti-cyclone asymmetry is often quantified using the skewness of $\omega_\parallel$, $Sk(\omega_\parallel) = [\omega_\parallel^3]/[\omega_\parallel^2]^{3/2}$, where $\omega_\parallel$ is the component of *fluctuating* vorticity parallel to the rotation axis. In this paper, we use [] to represent spatially averaged quantities. A positive skewness indicates a preference towards cyclonic vorticity for high values of $\omega_\parallel$ and this is what is observed in homogeneous rotating turbulence. A number of authors have considered the possible causes of this asymmetry. Turbulent flows under solid-body rotation have a natural tendency to develop positive values of $Sk(\omega_\parallel)$, as shown by a theoretical study reported in [7]. In addition, anti-cyclones with $\omega_\parallel \approx -2\Omega$ are susceptible to becoming unstable to the centrifugal instability while cyclones with similar magnitude of vorticity are stabilized, as argued in [1] and as confirmed by their direct numerical simulations (DNS) at varying values of the Rossby number. These results are confirmed by numerical simulations of an isolated cyclone or anti-cyclone in a rotating fluid [12], which show that at $Ro \sim 1$ cyclones are stable while anti-cyclones are unstable. This provides a possible explanation for the prevalence of cyclones in rotating turbulence at $Ro \sim 1$. Indeed, a number of studies have found that the maximum value of $Sk(\omega_\parallel)$ occurs at a Rossby number of order unity [13, 5].

In past experimental studies, to the best of the authors' knowledge, turbulence is either initiated in a rather homogeneous way and then allowed to decay, or it is maintained by some mechanism. Between the two, the former has been studied extensively, usually in a configuration whereby turbulence was generated by towing a grid through a container along the rotation axis and the rotating flow was then left to decay freely [10, 13, among others]. In these studies, the transient status of the flow, the formation and evolution of the columnar structures and their impact on the turbulence decay were the main focus. Examples of the latter include the pioneer experimental study [8], in which a periodically oscillatory motion was applied to a grid to force the turbulence to stay at a quasi-steady level. Common features of these experiments are that firstly turbulence can be introduced in a rather homogeneous manner as a start (essentially turbulence behind a grid); secondly, decay of physical quantities can be investigated in the decaying turbulence experiments and measurements can be made of the (reduced) energy decay rate; finally, bulk fluid rotation is made to a solid-body type, which was realised by putting the flow container on to a turn table.

In a recent experiment [6], both turbulence and bulk fluid rotation were generated in a very different way. The flow container was kept stationary and the rotation was onset and maintained by the co-rotation of two impellers installed at the top and the bottom of the container. Turbulence was generated by the relative motion of the fluid and the boundary. It was found that, although the flow motion was not a solid-body rotation and turbulence was not as homogeneous as one behind a towed grid (it was approximately homogeneous in the azimuthal direction), in the central region of the container where the background rotation is Rayleigh stable, similar features observed in previous experiments were evident: columnar eddies emerged and cyclonic eddies predominated the anti-cyclonic ones at $Ro \sim 1.5$, defined based on the local rotation rate $\Omega_r(r) = U_\theta/r$ (where U_θ is the mean azimuthal velocity and r is the local radius) and local integral length scale in the azimuthal direction $l_{u\theta}$, which can be calculated as

$$l_{u\theta}(r) = \int_0^{2\pi} \frac{\overline{u_\theta(\mathrm{r},\theta_0)\, u_\theta(\mathrm{r},\theta_0+\theta)}}{\overline{u_\theta^2(\mathrm{r},\theta_0)}} r \mathrm{d}\theta, \qquad (1)$$

where u_θ is the azimuthal component of the fluctuating velocity and overline denotes azimuthal average at a given r. $l_{u\theta}$ depends on r since turbulence intensity is inhomogeneous in the radial direction. Note that since the rotating flow is Rayleigh stable, viz. $\mathrm{d}(rU_\theta)/\mathrm{d}r > 0$, in the central region of the tank, the mean flow is not susceptible to the centrifugal instability in this region (see [6]). This

situation is similar to turbulence under solid-body rotation, in which the mean flow, $U_\theta = \Omega r$, is also Rayleigh stable (Ω is here a constant). However, the fluctuating velocity field may cause the turbulent flow to be locally unstable to the centrifugal instability. As a result, the mechanism described above leading to cyclone/anti-cyclone asymmetry could take place in this experiment, in the same way as it may be taking place in solid-body rotating turbulence. In addition, in this inhomogeneous experiment the Coriolis force still provides a restoring force that limits horizontal excursions of streamlines, which results in a form of inertial waves being present in this experimental configuration. Therefore, the idea of inertial wave propagation being responsible for columnar eddy formation, shaped by previous turn-table solid-body rotation experiments [3, 13], could be relevant also in the present flow. All in all, the non-solid-body rotating turbulence generated in this experiment in the central region of the tank resembles turbulence under solid-body rotation, at least qualitatively, and this was confirmed by the findings of our first study [6].

A limitation of the present experimental configuration is that the bulk rotation rate and the turbulence are created by the same mechanism, i.e. the co-rotating impellers and the interaction of the rotating flow with the baffles. As a result, the rotation rate and the turbulence intensity are correlated, and the fluctuating velocity approximately follows $[|u|] \propto \Omega$ (the impeller rotation rate). This means that the global Rossby number $Ro_G = [|u|]/(\Omega[l_{u\theta}])$ is not strongly dependent on Ω. Despite this, the value of Ro_G can be varied in our experiments by varying the number of baffles, which modifies $[|u|]$. Moreover, the inhomogeneous conditions lead to a local Ro that varies as a function of radius r and so interesting rotating flow dynamics arises. An important reason for choosing this experimental arrangement is that turbulence is maintained in a stationary manner without a mean decay. Therefore in addition to turbulence quantities [6], it also allows us to investigate the size and lifetime statistics of the organised eddies (both cyclonic and anti-cyclonic), which will be presented next.

2. Methodology

2.1. Experimental arrangement

The description of the facility and the optimisation of the experimental condition given the existing constraints have been presented and discussed in our previous work [6]. For readers' convenience, the sketch is re-presented in figure 1. The fluid container, which has a dodecagonal cross-section, is about 2000mm in both diameter (corner to corner) and height and is made of perspex of 15mm thick. Two impellers of $\varnothing \approx 1600$mm are mounted ≈ 100mm inward from the top and the bottom surface of the tank. Each impeller has eight blades of 150mm wide and 5mm thick. When the two impellers rotate at the same rate and direction, a bulk rotational environment can be generated. The rotation of the fluid in the central region is not solid-body type but is Rayleigh stable [6]. The four impeller rotational speeds Ω tested are 0.42 rad/s, 0.28 rad/s, 0.14 rad/s and 0.07 rad/s.

Ω	Ro_G			Re_G		
rad/s	B12	B6	B3	B12	B6	B3
0.42	3.35	2.38	1.78	5888	4623	2346
0.28	3.13	2.42	1.46	3694	3257	1544
0.14	2.91	2.30	1.38	1835	1679	826
0.07	3.17	2.21	1.44	882	836	354

Table 1: The Ro_G and Re_G over the entire flow field for all the cases, based on the velocity integral length scale $l_{u\theta}$. These are the spatial mean (global) quantities after ensemble averaging. Data taken from [6]

There are 12 baffles of Λ-shaped cross-section installed along each corner of the tank, which are the turbulence (vortex) generator. The number of baffles used (12, 6, 3 denoted as B12, B6 and B3), together with Ω, controls the turbulence intensity in the bulk fluid, hence the global Rossby number (Ro_G) and Reynolds number (Re_G), the range of which are tabulated in table 1, where Ro_G and Re_G are defined by the spatially averaged turbulence fluctuating velocity magnitude $[|u|]$, $[l_{u\theta}]$ and Ω.

A simple two-dimensional (2D) Particle Image Velocimetry (PIV) system, which consists of a Photron SA1 camera ($1024 \times 1024 \mathrm{pix}^2$) and a Gemini laser (Nd:YAG laser with 120mJ per pulse per cavity), is used to extract the 2D velocity information in the measurement plane, which is in the central part of the container, normal to the rotating axis and is about 450 mm $\times$ 450 mm. The PIV sampling rate is set at 45 samples per complete impeller revolution. The experimental duration for each testing case is 60.6 impeller revolutions which guarantees sufficient statistical convergence for the highest order turbulence quantities investigated in

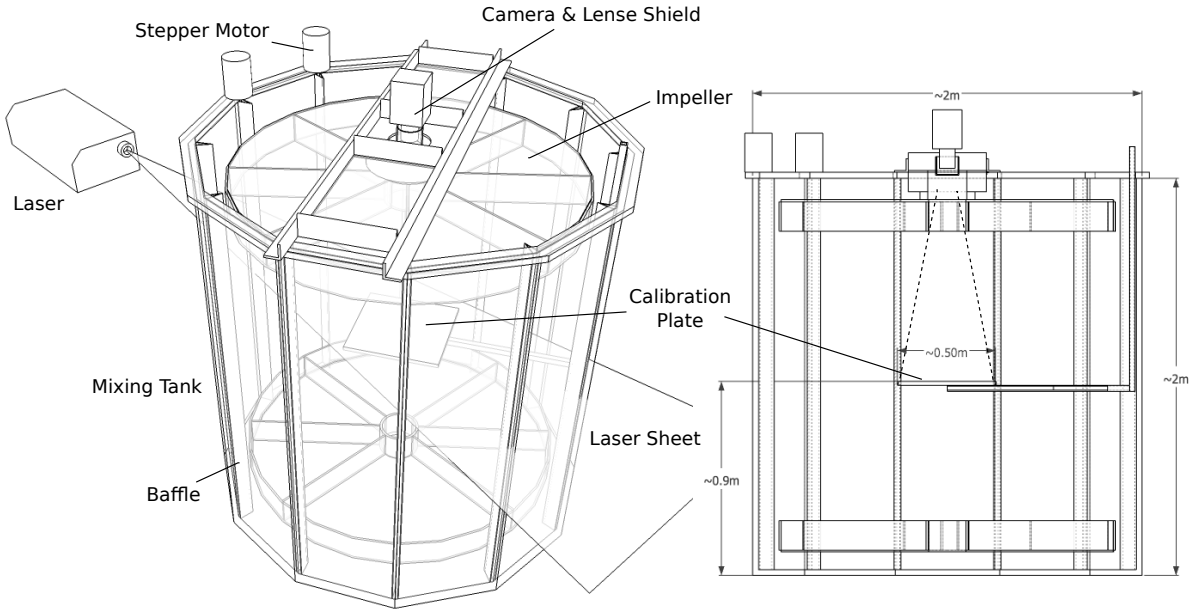

Figure 1: Schematic diagram of the experimental rig and the PIV measurement arrangement. Figure taken from [6].

this study. The spatial resolution based on the interrogation window size of the final pass (32×32 pix^2) is 14mm. The particle images are processed by DaVis 7.2.

2.2. Eddy identification scheme

An example of instantaneous *fluctuating* flow field (with the time-mean subtracted) is shown in figure 2 (a), which delineates the complexity of the eddy shapes, attributing to relatively high Re in the region. Determination of the eddy size can be approached from the streamline patterns or the vorticity shapes. However, neither of them is ideal, since firstly streamline geometries can vary significantly among eddies of the same type and secondly pearlescent flow visualisation in the vertical plane [6] suggests that a single columnar eddy may consist of multiple smaller winding eddies in the same spinning direction. It is for this reason that an eclectic approach is taken, which is illustrated in figure 2 and is briefly explained below.

As the preparation step, a uniform filter is applied to instantaneous vorticity $\omega_\parallel$ fields, followed by a non-linear median filtering process to remove the disorganised small background eddies. The uniform filter, the output of which being essentially a local spatial integration (with the support of the filter carrying the same weight), when applied to $\omega_\parallel$, leads to local circulation. That is, $\int_S \omega_\parallel \mathrm{d}s = \oint_C \mathbf{u} \cdot \mathrm{d}l$, where C encloses the filter kernel size S. The median filter is mainly to further reduce noise but preserve boundaries of $\omega_\parallel$ blobs. Kernel size $\sim [l_\omega]$ is chosen for both filtering processes, with $[l_\omega]$ being the spatial mean (through r) of the r dependent two-point-correlation of $\omega_\parallel$ [6], similar to equation 1,

$$l_\omega(r) = \int_0^{2\pi} \frac{\overline{\omega_\parallel(\mathrm{r}, \theta_0)\, \omega_\parallel(\mathrm{r}, \theta_0 + \theta)}}{\overline{\omega_\parallel^2(\mathrm{r}, \theta_0)}} r \mathrm{d}\theta. \qquad (2)$$

Because organised eddies tend to have relatively higher $\omega_\parallel$ magnitude and larger size, the filtering processes mainly remove small, fragmented, incoherent background eddies. An example of the filtering effect is shown in figure 2 (c). Compared to the instantaneous $\omega_\parallel$ field in (b), the processed field (c) contains less fragmented eddies. *Connected* $\omega_\parallel$ blobs are considered to be one organised eddy. One connected $\omega_\parallel$ region can be understood as a single 'island' on the basis of $|\omega_\parallel|$ threshold after filtering. It is introduced mainly to assist decision making on whether very close by vorticity blobs should be considered as fragments of the same eddy. The determination of their size and location is completed in the following three steps. The cyclonic and anticyclonic eddies are processed separately but in an identical way with the same parameter values.

S1 Regional $\omega_\parallel$ peaks are detected, but those too

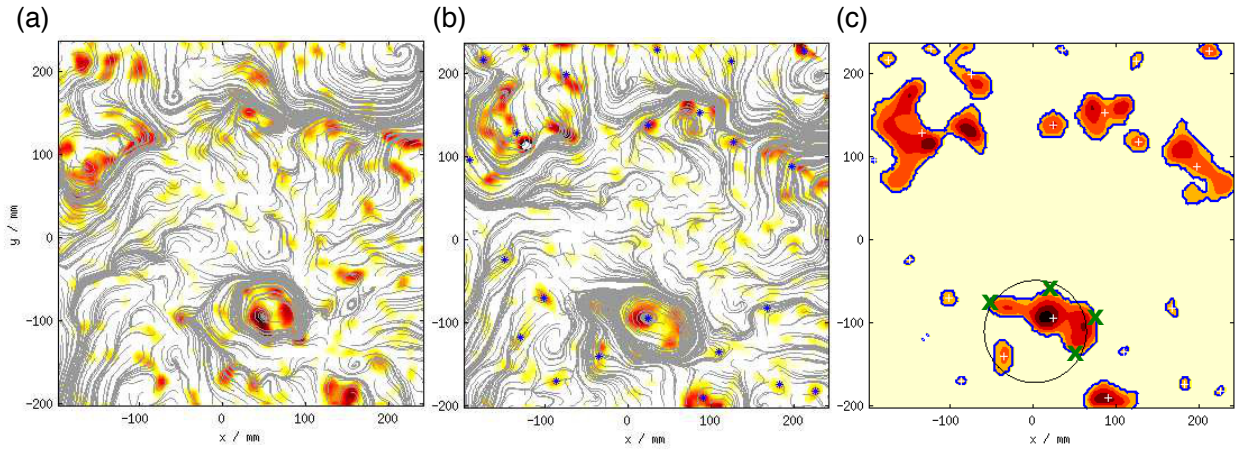

Figure 2: (a): A typical raw vorticity $\omega_{\parallel}$ and the associated streamline pattern taken from B12/0.42rad/s case, at an arbitrary time t_0; (b): same as (a) at $t_0 + \Delta t$, where Δt is the sample interval. Asterisks are the centroids of the selected eddies from (c). ; (c) the filtered $\omega_{\parallel}$ field of (b) and the circle fitting for one eddy, with $\times$ representing the (x, y) coordinate pairs of four maximum extent of the selected connected blob and $+$ the centroids of the eddies (asterisks in b); the *connected* eddy boundary is marked by thicker lines. In (a) and (b) contour levels for $|\omega_{\parallel}|$ are $[1 : 1 : 20]s^{-1}$. For clarification purpose, only the cyclonic eddies are shown. The anti-cyclonic eddies are treated in the same way.

close to the FOV margins or corners will not be further considered in the following steps. This is to avoid possible underestimation of eddy size.

S2 Connected $\omega_{\parallel}$ blobs enclosing those peaks are identified, which often contain more than one peaks. The coordinates of the $\omega_{\parallel}$ weighted centroids of such connected blobs $(x, y)_c$ are determined together with the coordinates of (typically three or four) points which define a rectangular envelope to represent the maximum extent of the blob, denoted as $(x, y)_{max}$. An example of the marked connected blob boundary, $(x, y)_c$ and $(x, y)_{max}$ are denoted by the thick line, $+$ and $\times$, respectively in figure 2 (c). $(x, y)_c$ are also marked in (b) as asterisks. The associated streamlines of some small vorticity blobs suggest shear-like regions rather than rotating eddies. However it may not be true owing to the (low) spatial resolution being similar to the eddy size.

S3 Based on $(x, y)_{max}$ of each connected blob, a circle is fit following the standard Levenberg-Marquardt scheme, which provides a reasonably accurate result and an acceptable computational convergence speed for processing large amount of data. The radius of the fitted circle is used to estimate the effective radius of the targeted eddy r_e. For any blob having three or four different $(x, y)_{max}$ pairs, a circular fit always exists. An example of fitting is shown in figure 2 (c). Although r_e may also be simply estimated by the area of the connected blob A_e, it is usually leads to an underestimation when compared to the corresponding streamline pattern. Furthermore, if the area of the fitted circle $A_c > \beta A_e$, the blob is disqualified to be a target eddy, since the large aspect ratio usually suggests a shear region. Here β is set to be 3.5. Albeit arbitrary, it does not discriminate between cyclonic and anti-cyclonic eddies. Note that eddy locations are still represented by $(x, y)_c$ based on A_e, but not the origin of the fitted circle.

3. Results and discussions

3.1. Size distribution of organised eddies

The number density distribution function of the eddy size, ρ_d, is presented in figure 3, where the cyclonic and anti-cyclonic eddies are processed separately but normalised by the total number of eddies detected. Note that ρ_d have the same shape as the individual PDFs of eddy size for cyclonic and for anti-cyclonic eddies. However, ρ_d is not the same as the PDF because of the different normalisation factor, meaning that it does not integrate to 1. Figure 3 shows that for eddies of both spinning directions, the majority are in size of $d \approx 0.02R_t$

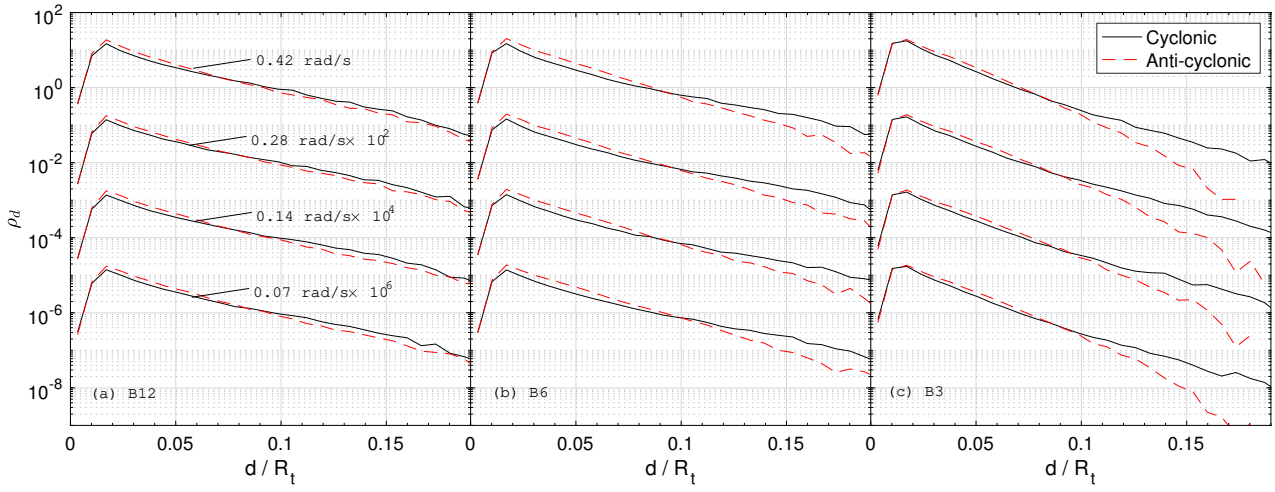

Figure 3: The number distribution function of eddy size, ρ_d. The distribution is normalised by the total number of organised (both cyclonic and anti-cyclonic) eddies detected. The lowest probability density shown refers to at least five events. For clarification purpose, cases 0.28 rad/s, 0.14 rad/s and 0.07 rad/s are shifted downwards by 2, 4 and 6 decades respectively.

($d = 2r_e$). Among eddies of $d > 0.02R_t$, there are much more small eddies than large ones. For eddies having $d \gtrsim 0.1R_t$, the number distribution of cyclonic eddies starts to overtake anti-cyclonic ones, with the difference becoming greater as d increases. Whereas, for $d \lesssim 0.08R_t$, number distribution is reversed, but only marginally. It explains the non-zero cyclonic skewness of $\omega_\parallel$ observed previously. Note $\sum \omega_\parallel = 0$, since $\omega_\parallel$ is the fluctuating component. The slopes of the (semi-log) ρ_d lines for $d \gtrsim 0.1R_t$ are steeper when the baffle number reduces. For example in B3, chances to see eddies of $d \approx 0.1R_t$ of both sense are rarer than that in B12 and B6 case relatively. Results in section 3.2 will show that regardless of the shapes of the many small eddies, the majority play a transient role in the flow.

Figure 4 (a) shows the dependence on Re_G of the so-called characteristic eddy size $d^* \sim 0.09R_t$, at which the number of cyclonic and anti-cyclonic eddies is approximately the same. It is determined by the (only) intersection point of the two ρ_d lines in figure 3 for each testing case. This means that there are more cyclonic eddies than anti-cyclonic ones for size $> d^*$. As Re_G increases, d^* weakly declines from 0.1 to 0.08 R_t. If conditional averaged u and $\omega_\parallel$ is applied to the eddies of size d^*, denoted as $\langle u^* \rangle$ and $\langle \omega_\parallel^* \rangle$ respectively, the characteristic macro and micro-Ro, denoted as $\langle u^* \rangle / (\Omega_r d^*)$ and $\langle \omega_\parallel^* \rangle / \Omega_r$ respectively, can be obtained. In this paper we use $\langle\rangle$ to denote conditional averaged quantities. Here the local $\Omega_r(r)$ is used, which is derived from $U_\theta(r)$ distribution given in figure 4 of [6]. The radius r here is that of the centre of the eddy of size d^* under scrutiny. It is evident in figure 4 (b) and (c) that over the examined Re_G range, as it increases, the averaged characteristic macro-Ro and micro-Ro increase, even though cases B6 and B12 are close to each others. Experiments with 3 baffles tend to have a smaller Reynolds number Re_G and Rossby number Ro_G than the cases B6 and B12. Indeed, flow visualisations showed that the B3 cases at lower rotation rates were not highly turbulent and appeared to be chaotic but viscously-dominated flows without significant small scales.

Moving towards high-Re_G curves, the Rossby number demarcating cyclonic from anti-cyclonic eddy dominance approaches $Ro^* = \langle u^* \rangle / (\Omega_r d^*) \approx 2$ and $Ro_\omega^* = \langle \omega_\parallel^* \rangle / \Omega_r \approx 8$ asymptotically. It is therefore expected that for an eddy of size d whose Rossby number $\langle u \rangle / (\Omega_r d) < Ro^* \approx 2$, there would be a clear asymmetry between cyclones and anti-cyclones (i.e. this eddy will tend to be a cyclone). This demarcation Rossby number Ro^* is consistent with our first study [6], in which we found that the maximum vorticity skewness occured at $Ro(r) \approx 1.5$. The value of Ro^* is also consistent with a study of isolated vortices under solid body rotation [12] which found that cyclones are stable while anti-cyclones are unstable at $Ro \sim 1$. A num-

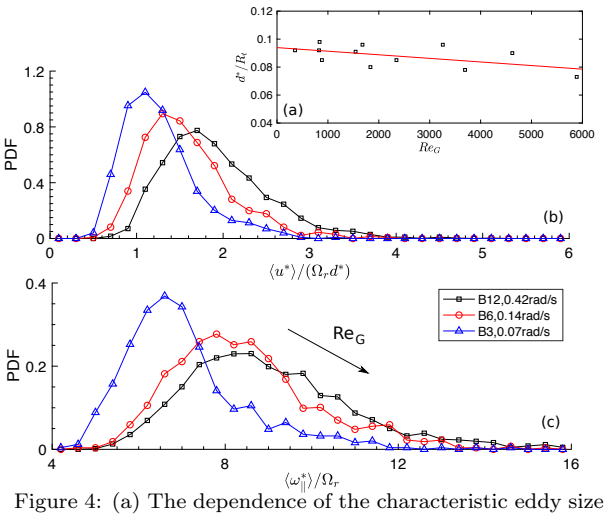

Figure 4: (a) The dependence of the characteristic eddy size d^* on the global Reynolds number Re_G; (b) and (c) the PDF of the conditional averaged macro- and micro-Ro for eddies at size d^*, for cyclonic eddies. Cases of the maximum, the minimum and an intermediate Re_G are shown. The nearly identical PDF of the anti-cyclonic eddies is not shown.

ber of studies have also found the maximum vorticity skewness in solid-body rotating turbulence to occur at a Rossby number close to unity [13, 5]. This correspondence with results of turbulence under solid body rotation at $Ro \sim 1$ is remarkable and it likely means that the same mechanisms leading to cyclone/anti-cyclone asymmetry are at work. Hence, even in the present experiment, it should be the greater susceptibility of anti-cyclones to the centrifugal instability that is responsible for the asymmetry (as discussed in Refs. [1, 12]).

In order to know the locational distribution of eddies, joint probability density functions (JPDF) between d and their radial location r are shown in figure 5. It was found that curves of different impeller rotation rate Ω nearly collapse for both cyclonic and anti-cyclonic eddies (figure not shown), which suggests that d distribution is almost independent of Ω. It is for this reason that quantities are averaged over the four Ω and are given as a function of baffle number only. To obtain the number density, a weighting function based on the local available area needs to be applied, due to the square FOV near the corners. It can be seen from figure 5 that for $r \lesssim 0.25R_t$, chances are more to see large cyclonic eddies at a fixed r than anti-cyclonic ones. Provided r is not too close to the corners of the FOV, where the local area is too small for any eddy to be completely detected, some useful information can be drawn.

The lowest contour level in figure 5 represents at least ten eddies. The 'hill' shaped contours have a 'valley' near $r \approx 0.22R_t$ which is probably attributed to the weighting function having its maxima near the same place (about the half side size of the square FOV). Both B12 and B6 cases have a small region of $N = -2$ contour near $r \approx 0.12R_t$ for anti-cyclonic eddies, which infers that we have less chance to find very small cyclonic eddies at $r \approx 0.1R_t$. This is in line with the excessive anti-cyclonic eddies shown in figure 3. Notwithstanding the rather small FOV of this experiment, the location of the highest density of large eddies (the peaks of the hills) was captured at $0.15 \lesssim r/R_t \lesssim 0.2$.

Figure 5 also shows that the peak of the cyclonic hill generally does not locate at the place where they are dominant, to the maximum extent, over the anti-cyclonic ones. That is, large anti-cyclonic eddies are often detected in the vicinity of the large cyclonic ones, resulting in the local $\omega_\parallel$ not necessarily highly skewed. In B12 case for instance, the largest population of large d for both cyclonic and anti-cyclonic eddies is at $r \approx 0.15R_t$. We defer further discussions about this point.

If we perform an integration along a fixed r in figure 5, the local averaged eddy size $\langle d \rangle = \langle d\,(r) \rangle$ will be obtained and the result is given in figure 6. The dip at $r \approx 0.22R_t$ in each plot corresponds to the one appearing in figure 5. Since it is believed to be an artefact of the weighting function, a polynomial fit is applied to represent the trend of $\langle d \rangle$. The fitting function is only shown for the cyclonic eddies, which indicates that the maximum $\langle d \rangle$ moves to larger r from B12 to B3 and its magnitude declines.

The Rossby number based on the local integral length scale $l_{u\theta}$ in the azimuthal direction (equation 1), $Ro\,(r)$, has been discussed previously [6]. Here the effect of the individual eddy sizes d on $Ro\,(r)$ can be evaluated. Only $\langle d \rangle$ of the cyclonic eddies are used. The local rotation rate $\Omega_r\,(r)$ and the local fluctuating velocity $u_r\,(r)$ obtained previously still applies. The Rossby number $Ro\,(r)$ based on $\langle d \rangle$ is hereby denoted as $Ro\langle d, \Omega_r \rangle = u_r/(\Omega_r \langle d \rangle)$ and is given by figure 7 (b), while the variation on r of the skewness of $\omega_\parallel$, $Sk(\omega_\parallel)$, is taken from [6]. A polynomial fit has been applied to the Ω averaged $Sk(\omega_\parallel)$, after a low pass filter by a kernel size $\sim [l_\omega]$; see also § 2.2.

Some observations that can be made in figure 7 are that firstly, when the local d and Ω_r are ap-

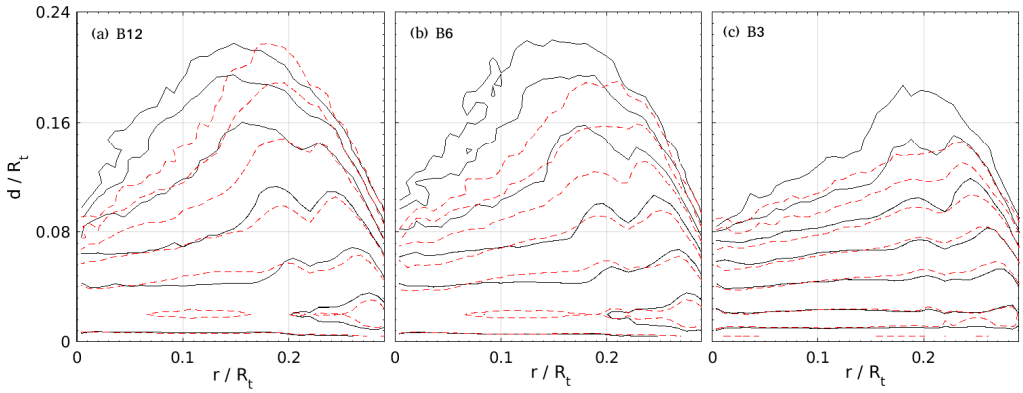

Figure 5: The JPDF for the local eddy number density, between eddy size d and radial location r. Contours marked by $-$ denote cyclonic eddies; those marked by $--$ denote anti-cyclonic ones. Contour level: 10^N, where $N = -4.5 : 0.5 : -2$. Probability for $N < -4.5$ is not shown.

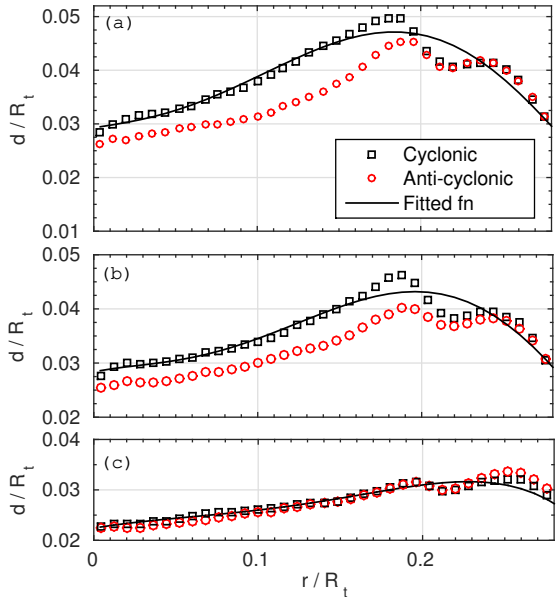

Figure 6: The dependence of local mean eddy size $d(r)$ on the radial distance r. Polynomial fitting functions for the cyclonic curve are also shown. (a) B12, (b) B6, (c) B3.

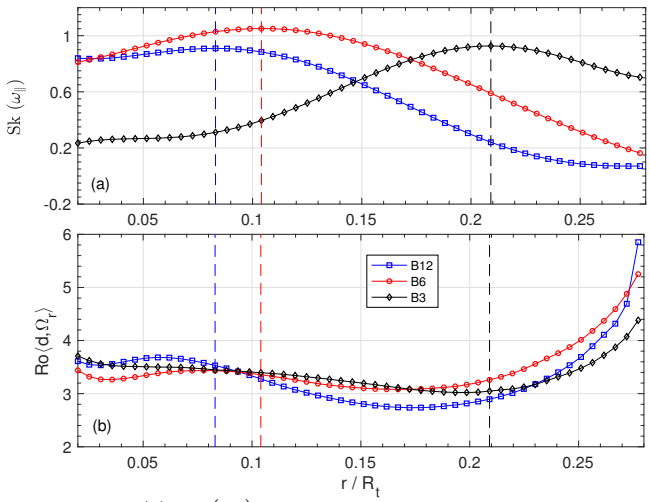

Figure 7: (a) $Sk\left(\omega_{\parallel}\right)$ averaged over the four Ω at a given baffle number. (b) $Ro\langle d, \Omega_r\rangle$ based on the local averaged eddy size $d(r)$ and local flow rotation rate $\Omega_r(r)$. The r locations of $Sk\left(\omega_{\parallel}\right)_{max}$ are denoted by dashed lines.

plied, $Ro\langle d, \Omega_r\rangle$ spontaneously falls into the range $2.75 \sim 3.75$, for $r \leq 0.22R_t$. Note that this is unlike $Ro\,(r)$ based on the local integral length scale which has no constant plateau but monotonically grows with r (the integral length scale $l_{u\theta}$ contains also small incoherent eddies). Secondly, the maximum skewness $Sk\left(\omega_{\|}\right)_{max}$ in (a) locate at r corresponding to $Ro\langle d, \Omega_r\rangle \approx 3.0 \sim 3.5$. Furthermore, returning to figure 5, which shows that cyclonic eddies are dominant in large d (see the lowest contour levels $N = -4.5$ and -4, for example) and the maximum extent of this dominance is found at $r \approx 0.08R_t, 0.1R_t, 0.18R_t$, for the three baffle number cases respectively, which again correspond to $Ro\langle d, \Omega_r\rangle \approx 3.0 \sim 3.5$. From these results, an interesting remark can be made regarding the size of the cyclones. For all experiments (even B3 cases at low Re_G), the size of cyclones tends to be self-adjusted to $\langle d\rangle \approx u_r/(2.75{\sim}3.75)\Omega_r \approx (0.3{\sim}0.4)u_r/\Omega_r \approx const$, independent of radial position for $r \leq 0.22R_t$. In other words, the size of cyclonic eddies is fixed by the local value of u_r/Ω_r, and so $\langle d\rangle \sim u_r/\Omega_r$.

3.2. The lifetime of the organised structures

Having identified the sizes and the locations of the organised eddies in each snapshot, the temporal resolution of the experiment allows a track of their evolution, from which their lifetime can be estimated. The equivalent angular resolution is $\Delta\phi = 2\pi/45 = 0.14$. Figure 8, together with figure 2, provide an example of early to middle age of a cyclonic eddy. The evolution of the eddy size d is also shown. This particular eddy is born at a medium size $d \approx 0.1R_t$ at an arbitrarily defined $\phi = 0$. Its size keeps changing by interacting with the surrounding vorticity blobs as it moves with the bulk rotation. The eddy identification scheme introduced in § 2.2 suggests that after the low-pass filtering process the eddy indicated in (a) is an elongated but connected zone (figure not shown), as also indicated by the irregular but foci-type streamline shapes. Soon after $\Delta\phi$, it is broken into two adjacent separated vorticity blobs, as shown in b, with one of which highlighted. It must be admitted that considering its past and future (a and c), the eddy highlighted in (b) with $d \approx 0.07R_t$ is probably one of the two winding eddies forming a large pair, which should be considered as a single large eddy of $d \approx 0.12R_t$. However, the current eddy detection scheme has treated it to be a standalone structure. As an isolated snapshot, it is difficult to judge from the vorticity or/and streamline pattern whether it is a separated eddy or not. After another $\Delta\phi$, the eddy evolves to be the one shown in (c), where the two nearby eddies in (b) merge. Sample episodes of its later life are indicated by (d) and (e) and they are shown in figure 2 (a) and 2 (b) respectively. Soon after (e), its size starts to decline and finally it disappears in the background turbulence at a size $\approx 50mm$ at $\phi \approx 2.5$.

The eddy tracking scheme can be summarised into three steps. Similar to the identification scheme, cyclonic and anti-cyclonic eddies are processed separately.

S1 Consider two sequential snapshots $\mathcal{A}$ and $\mathcal{B}$ separated by $\Delta\phi$, eddy centroid coordinates in $\mathcal{A}$, denoted as $(x, y)^I_{\mathcal{A}}$, are determined by the identification scheme discussed in section 2.2. From the mean local rotation rate $\Omega_r\,(r)$, we can predict their new location in $\mathcal{B}$, $(x, y)^P_{\mathcal{B}}$.

S2 Similarly, identification scheme also finds $(x, y)^I_{\mathcal{B}}$ in $\mathcal{B}$. The common elements in $(x, y)^P_{\mathcal{B}}$ and $(x, y)^I_{\mathcal{B}}$ are the eddies which survive from $\mathcal{A}$ to $\mathcal{B}$. Whereas the elements in $(x, y)^P_{\mathcal{B}}$ but not in $(x, y)^I_{\mathcal{B}}$ are the ones broken or dissipated and the elements in $(x, y)^I_{\mathcal{B}}$ but not in $(x, y)^P_{\mathcal{B}}$ are the ones newly formed in $\mathcal{B}$. Due to relatively high turbulence level, relaxation is needed for searching the common elements in $(x, y)^P_{\mathcal{B}}$ and $(x, y)^I_{\mathcal{B}}$. That is, a discrepancy of (x, y) within a small distance Δl is accepted.

S3 For each match pair, a further check of the eddy size difference is performed. After an allowable range Δd is defined, if the matched eddy size $d_{\mathcal{B}}$ drops below $d_{\mathcal{A}} - \Delta d$, the life of its match in $\mathcal{A}$ is considered terminated and the one in $\mathcal{B}$ is considered as newborn. If $d_{\mathcal{B}}$ goes beyond $d_{\mathcal{A}} + \Delta d$, then most probably it has merged with a neighbour eddy. In such a case, its match in $\mathcal{A}$ is also considered terminated and itself is treated either as the continuous life of its neighbour's or as newborn.

The choices of Δl and Δd mainly depend on the turbulence level of each case, or Re_G. The tracking scheme is only applied to eddies whose location $r \lesssim 0.2R_t$, to avoid bias to shorter lifetimes due to FOV availability.

Similar to ρ_d for eddy size, the number density distribution function for eddy lifetime, ρ_T, is shown

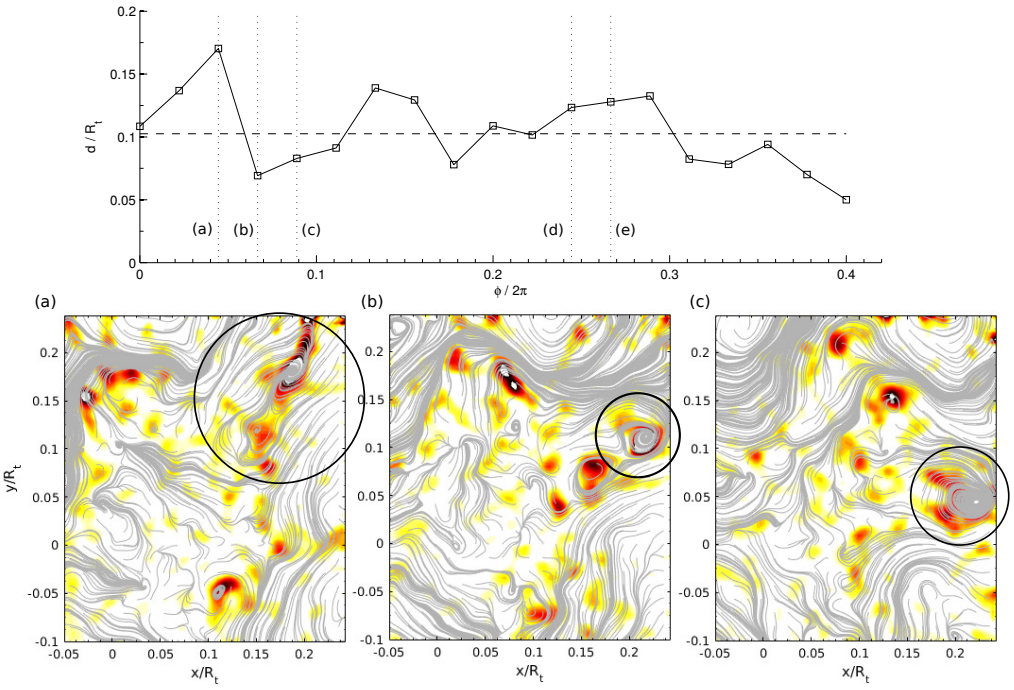

Figure 8: The variation of the size d of a typical cyclonic eddy in B12/0.42rad/s case during its life cycle represented by ϕ, the angular displacement it covers. Note that the bulk fluid rotation is clock-wise. The $--$ line indicates its mean size; the vertical $\cdot\cdot$ lines mark five instants in its life. In (a) (b) & (c) the eddy being looked at is highlighted by a circle; (d) refers to the eddy at $(50, -100)$mm in figure 2 (a); (e) refers to the same eddy in figure 2 (b).

in figure 9. It can be seen that the majority have short lifetime, perceivable in only one snapshot. Nevertheless, some eddies remain alive for nearly half a flow revolution. Cyclonic eddies tend to survive longer than anti-cyclonic ones, with lifetime difference becoming clearer as $\phi > 0.2 \times (2\pi)$. In comparison, the angular displacement of a turbulent eddy $\phi_{nl} \sim \Omega t_{nl} \sim 1/Ro$ (where $t_{nl} \sim l/u$, is the turbulent eddy turn-over time) is typically $(0.05 \sim 0.1) \times (2\pi)$, which is approximately one order of magnitude smaller. Note that the discrete PIV sampling leads to an intrinsic uncertainty in lifetime counting. The angular coverage of an eddy for its entire life is counted as $N\Delta\phi$, with an uncertainty of $\pm\Delta\phi$, where N is the number of snapshots in which it is captured.

In terms of the absolute lifetime T (in seconds), it is reassuring that some long-lived eddies, both cyclonic and anti-cyclonic, have their T in the same order of magnitude as the (spatially averaged) integral eddy turn over time in the flow field $l_{u\theta}/u$ and an order of magnitude larger than the characteristic eddy turn over time scale $1/\omega_{\|}^{*}$ (conditioned based on d^{*}). While the angular coverage ϕ of the eddies are similar regardless of baffle number and impeller angular velocity, apparently the dimensionless T depends on the baffle number. This is because, by and large, for the global turbulence level $B12 > B6 > B3$, which results in the reversed order for eddy turn over time, both $[l_{u\theta}/u]$ and $\langle 1/\omega_{\|}^{*} \rangle$.

Similar to the characteristic eddy size d^{*}, the eddy characteristic lifetime T^{*} can be described as the lifetime at which there are equal number of cyclonic and anti-cyclonic eddies. That is, it is the demarcation beyond which there are larger proportion of long lived cyclonic eddies than anti-cyclonic ones, and it can be obtained from figure 9 by finding the intersection of the ρ_T lines. The T^{*} for all the testing cases are shown in figure 10, which shows its relation to the two time scales of the characteristic eddies. It is clear that T^{*} scales with the turn over time of the characteristic eddy d^{*}/u^{*} and is about one order of magnitude larger than the time scale $1/\omega_{\|}^{*}$. Perhaps not surprisingly, T^{*} also decreases as Re_G increases.

If the joint PDF of T (or ϕ) and d is examined (figure not shown), the dependence of T on d can

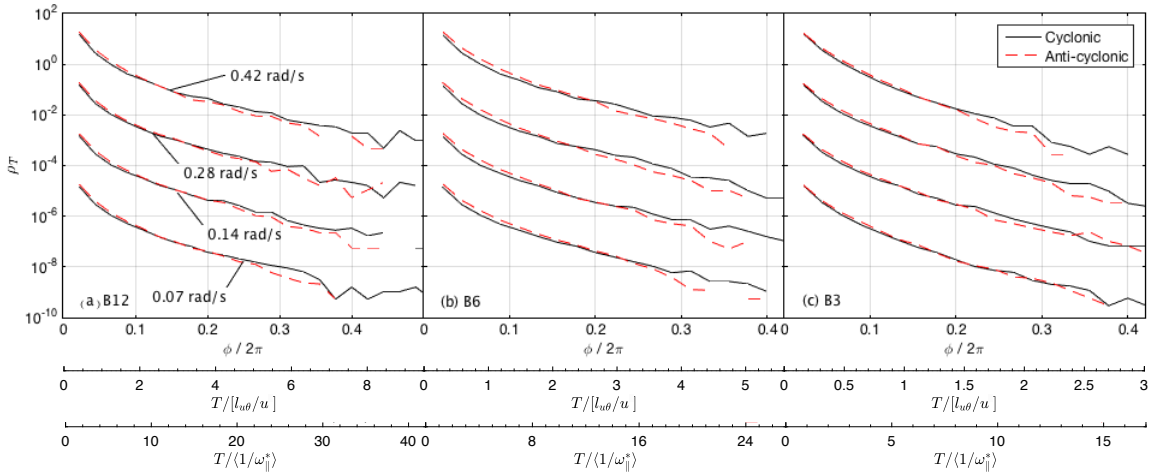

Figure 9: The number density function for eddy lifetime, ρ_T, in terms of the angular coverage ϕ and the absolute time T. Cases 0.28 rad/s, 0.14 rad/s and 0.07 rad/s are shifted downwards by 2, 4 and 6 decades respectively.

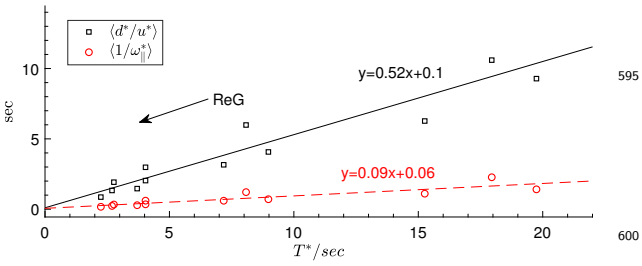

Figure 10: Eddy characteristic lifetime T^*.

be obtained and it is shown in figure 11. The abscissa is normalised by d^* and the ordinate is normalised by the time scale $\langle l_{u\theta}/u \rangle$ and Ro_G, which results in the best data collapsing after many trials. Note that $\langle T \rangle$ here is the averaged lifetime for a given eddy size d; $\langle l_{u\theta}/u \rangle$ is lifetime averaged on individual coherent eddies detected by the lifetime counting algorithm and Ro_G is a spatially averaged global quantity (see table 1). Similar to figure 5, there are many eddies which have short lifetime. Interesting information that can be extracted from figure 11 are that firstly, for small eddies, regardless of the direction of spin, eddies' normalised lifetime is proportional to their size d, with a scaled slope of about 0.37 for the dimensionless quantities. For $d \lesssim d^*/2$, it is also independent of the baffle number. Secondly, for $d \gtrsim d^*$, separation of T among cyclonic and anti-cyclonic eddies becomes evident. At $d \approx 1.2d^*$, ΔT $(=T_c - T_{anti-c})$ is approximately maximum. Also at $1.2d^*$, eddy lifetime T starts to be a decreasing function of size d. Thirdly, T_{max}, though normalised, still displays a baffle number dependent behaviour, viz. $T(B12) > T(B6) > T(B3)$, which perhaps is counter-intuitive, in the sense that the longest lifetime occurs at larger Re_G flows; see also figure 9 (a). The exact reason is not clear, but it seems that ΔT_{max} is consistent with the Re_G magnitude.

4. Conclusions

This paper follows our previous 2DPIV experimental investigation of a rotating turbulence in a unique configuration which allows us to access the statistics of both cyclonic and anti-cyclonic eddies and their evolution in a stationary turbulence environment. That is, the amount of turbulence is maintained at a constant level throughout the experiments. Due to the location of the turbulence generator (baffles), the inhomogeneous turbulence in the radial direction also induces radial variation of quantities, e.g. local Ro. The measurement is conducted in the central region of the tank, which, although not of a solid-body rotation, is Rayleigh stable. The relatively large depth to diameter ratio of the facility reduces the constraint of columnar eddy growth in the axial direction.

This study addresses the direct account for eddy sizes, their density and lifetime distribution by

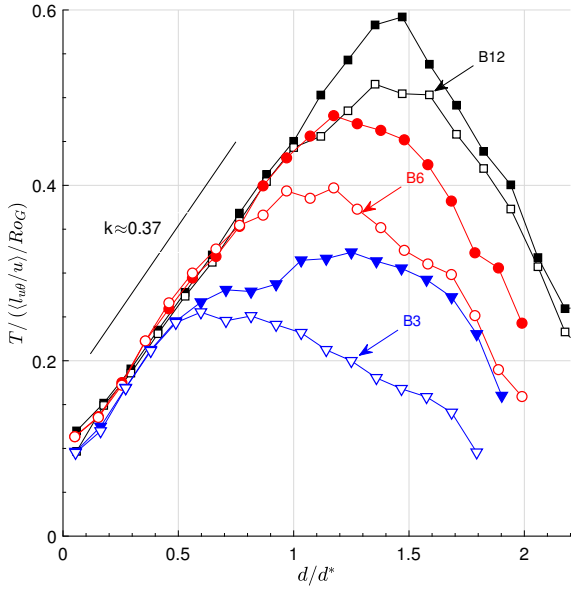

Figure 11: Dependence of averaged eddy lifetime T on eddy size d. Filled symbols are for cyclonic eddies and open symbols for anti-cyclonic eddies. The dependence on the impeller speed is found to be very small and therefore data are averaged through the four impeller speeds.

proposing an eddy detection scheme followed by an algorithm to estimate lifetime. The results suggest that eddy size $0.08R_t \lesssim d \lesssim 0.1R_t$ seems to be a separation of statistical counts for cyclonic and anti-cyclonic eddies, which is denoted as the characteristic eddy size d^*, and is found to be a weak decreasing function of the global Reynolds number Re_G. For larger eddies of $d \gtrsim d^*$, the cyclonic eddies are noticeably dominant over the anti-cyclonic ones in terms of number density and lifetime T; while for $d \lesssim d^*$, the latter are prevalent, but only marginally. In other words, large eddies with size $d > d^*$ tend to be cyclonic and large cyclonic eddies are more long-lived than large anti-cyclonic eddies. Some eddies are found to be as large as $\sim 3d^*$, but these eddies are generally as transient as those with $d < d^*$. The longest lived eddies, which are observed in B12 cases, are found to live nearly an order of magnitude longer than the averaged integral eddy turn over time $l_{u\theta}/u$ of those cases, with some of which being able to cover 40% of a flow revolution.

The characteristic eddy lifetime T^*, being the time over which more cyclonic eddies live longer than the anti-cyclonic ones, is found to scale with the characteristic eddy turn over time d^*/u^*. It has also been shown that for eddies of $d \lesssim d^*/2$, the normalised T is linearly correlated with d/d^* and T_{max} occurs at $d \approx 1.2d^*$. For eddies of $d \gtrsim d^*$, the excess of lifetime of cyclonic eddies is also evident. It must be stressed that the current experimental method cannot tell whether the eddies discussed here are columnar shaped or not, but figure 9 does show that a significant portion of the eddies detected has T which is an order of magnitude larger than the turbulence eddy turn over time.

The macro- and micro-Ro, based on the conditional averaged quantities over the characteristic eddies of size d^*, show weak increment following Re_G. For the high-Re_G cases, the demarcation macro-Ro is $Ro^* \approx 2$, which is consistent with a previous study of eddies in solid body rotation [12]. This is suggestive of anti-cyclones being destabilized by the centrifugal instability at $Ro \sim 1$ also in the present non-solid-body rotating turbulence experiment. It is expected that this is the cause of the observed cyclone/anti-cyclone asymmetry.

Using the local mean eddy size $\langle d\rangle$ (with the background turbulence eddy removed) and local flow rotation $\Omega_r(r)$, the local Rossby number $Ro\langle d, \Omega_r\rangle$ is spontaneously adjusted to $2.75 \sim 3.75$ in the central rotation region. This means that for all radii in the central region, the average cyclone size is approximately proportional to the local value of u_r/Ω_r, viz. $\langle d\rangle \sim u_r/\Omega_r$. The radius where the maximum $Sk(\omega_\parallel)$ is observed corresponds to $3.0 \lesssim Ro\langle d, \Omega_r\rangle \lesssim 3.5$. Compared to the corresponding $l_{u\theta}$ defined $Ro(r)$, which is ~ 1.5, the slightly larger value is due to the different length scale used, viz. $\langle d\rangle \lesssim l_{u\theta}$. However, since $l_{u\theta}$ does not remove the contribution from the background incoherent eddies, no spontaneous lock of $Ro(r)$ to $\approx const$ value can be observed.

Finally, it must be mentioned that the eddy detection and lifetime estimation techniques, apparently are not entirely objective, since they depend on empirical parameters: the shape threshold for eddy detection β, Δl and Δd for lifetime estimation. This is mainly owing to the highly distorted eddy shapes in relatively high Re_G and Ro_G flow environment. However, they do not discriminate between cyclonic and anti-cyclonic eddies, and therefore are objective in this respect. That is, since the cyclonic and anti-cyclonic vorticities are processed separately and with the same parameters, there should be no bias towards either of them.

References

[1] Bartello, P., Métais, O. & Lesieur, M. 1994 Coherent structures in rotating three-dimensional turbulence *J. Fluid Mech.* **273**, 1–29

[2] Davidson, P. A. 2004 Turbulence *Oxford University Press* New York

[3] Davidson, P. A., Staplehurst, P. J. & Dalziel, S. B. 2006 On the evolution of eddies in a rapidly rotating system. *J. Fluid Mech.* **557**, 135–144

[4] Davidson, P. A., Kaneda, Y. & Sreenivasan, K. 2013 Ten chapters in turbulence *Cambridge University Press* Cambridge

[5] Deusebio, E., Boffetta, G., Lindborg, E. & Musacchio, S. 2014 Dimensional transition in rotating turbulence *Phys. Rev. E* **90**, 023005

[6] Gan, L., Baqui, Y.B. & Maffioli, A. 2016 An experimental investigation of forced steady rotating turbulence. *Eur. J. Mech. B/Fluids* **58**, 59–69

[7] Gence, J.-N. & Frick, C. 2001 Naissance des corrélations triples de vorticité dans une turbulence statistiquement homogène soumise à une rotation *C. R. Acad. Sci. Paris*, Ser. II b, **329**, 351–356

[8] Hopfinger, E. J., Browand, F. K. & Gagne, Y. 1982 Turbulence and waves in a rotating tank. *J. Fluid Mech.* **125**, 505–534

[9] Kolvin, I., Cohen, K., Vardi, Y., & Sharon, E. 2009 Energy transfer by inertial waves during the buildup of turbulence in a rotating system. *Phy. Rev. Lett.* **102**, 014503

[10] Morize, C., Moisy, F. & Rabaud, M. 2005 Decaying grid-generated turbulence in a rotating tank. *Phys. Fluids* **17**, 095105

[11] Smith, L. M. & Waleffe, F. 1999 Transfer of energy to two-dimensional large scales in forced, rotating three-dimensional turbulence. *Phys. Fluids* **11**(6), 1608–1622

[12] Sreenivasan, B., & Davidson, P. A. 2008 On the formation of cyclones and anticyclones in a rotating fluid. *Phys. Fluids* **20**(8), 085104

[13] Staplehurst, P. J., Davidson, P. A. & Dalziel, S. B. 2008 Structure formation in homogeneous freely decaying rotating turbulence. *J. Fluid Mech.* **598**, 81–105

[14] Waleffe, F. 1993 Inertial transfers in the helical decomposition. *Phys. Fluids A* **5**(3), 667–685